

## Atomic-scale visualization of *d*-wave altermagnetism

Daran Fu,<sup>1,2†</sup> Liu Yang,<sup>3†</sup> Kebin Xiao,<sup>1,2</sup> Yuyang Wang,<sup>1,2</sup> Zhiwei Wang,<sup>3,4,5\*</sup> Yugui Yao,<sup>3,4,5</sup> Qi-Kun  
Xue,<sup>1,2,6,7,8\*</sup> and Wei Li<sup>1,2,8\*</sup>

<sup>1</sup>*State Key Laboratory of Low-Dimensional Quantum Physics, Department of Physics,  
Tsinghua University, Beijing 100084, China*

<sup>2</sup>*Frontier Science Center for Quantum Information, Beijing 100084, China*

<sup>3</sup>*Centre for Quantum Physics, Key Laboratory of Advanced Optoelectronic Quantum  
Architecture and Measurement (MOE), School of Physics, Beijing Institute of Technology,  
Beijing 100081, China*

<sup>4</sup>*Beijing Key Lab of Nanophotonics and Ultrafine Optoelectronic Systems, Beijing Institute of  
Technology, Beijing 100081, China*

<sup>5</sup>*International Center for Quantum Materials, Beijing Institute of Technology, Zhuhai,  
519000, China*

<sup>6</sup>*Beijing Academy of Quantum Information Sciences, Beijing 100193, China*

<sup>7</sup>*Southern University of Science and Technology, Shenzhen 518055, China*

<sup>8</sup>*Hefei National Laboratory, Hefei 230088, China*

\*To whom correspondence should be addressed: [zhiweiwang@bit.edu.cn](mailto:zhiweiwang@bit.edu.cn);  
[qkxue@mail.tsinghua.edu.cn](mailto:qkxue@mail.tsinghua.edu.cn); [weili83@tsinghua.edu.cn](mailto:weili83@tsinghua.edu.cn)

Altermagnetism is a newly discovered fundamental form of magnetic order, distinct from conventional ferromagnetism and antiferromagnetism<sup>1</sup>. It uniquely exhibits no net magnetization while simultaneously breaking time-reversal symmetry<sup>2-6</sup>, a combination previously thought to be mutually exclusive. Although its existence and signatures in momentum space have been established<sup>2,7-13</sup>, the direct real-space visualization of its defining rotational symmetry breaking has remained a missing cornerstone. Here, using scanning tunnelling microscopy, we present atomic-scale imaging of electronic states in the candidate material CsV<sub>2</sub>Se<sub>2</sub>O. We directly visualize the hallmark symmetry breaking in the form of unidirectional electronic patterns tied to magnetic domain walls and spin defects, as well as elliptical charging rings surrounding those defects. These observed electronic states are all linked to the underlying alternating spin texture. Our work provides the foundational real-space evidence for altermagnetism, moving the field from theoretical and momentum-space probes to direct visual confirmation; thereby opening a path to explore how this unconventional magnetic order couples to and controls other quantum electronic states.

Altermagnetism has emerged as a third elementary category of magnetic order, completing the established dichotomy of ferromagnetism and antiferromagnetism<sup>1,3,14</sup>. Its defining characteristic is the coexistence of a vanishing net magnetization, akin to antiferromagnets, with a broken time-reversal symmetry, a hallmark of ferromagnets<sup>2-6</sup>. This unique blend arises from specific crystal symmetries where the arrangement of non-magnetic atoms imposes an environment that forces a crystallographic rotation, rather than a simple translation, to connect the spin-up and spin-down sublattices (Figs. 1a, b)<sup>1,15</sup>. This underlying symmetry breaking is predicted to produce alternating spin polarizations in both real and momentum space, leading to novel phenomena such as non-zero Berry curvature, anomalous Hall effects and momentum-dependent spin splitting, which have spurred significant research interest for both fundamental physics and potential applications<sup>2-7,14-28</sup>.

The formal classification of this phase relies on the non-relativistic spin group theory, which treats transformations in spin space and real space independently<sup>14,29-33</sup>. In this framework, altermagnetism is described by a combined operation  $[R_i||R_j]$ , coupling a rotation in spin space to a distinct rotation in real space<sup>14</sup>. This differs fundamentally from conventional ferromagnetism (a single spin lattice) or antiferromagnetism (spin sublattices linked by translation or inversion). The consequential reduction in point group symmetry for each spin sublattice, for example, from four-fold ( $C_4$ ) to two-fold ( $C_2$ ), is the root cause of the anisotropic, alternating spin-polarized bands observed in reciprocal space<sup>1,3,7-13</sup>. Despite these well-established momentum-space signatures and theoretical predictions, the direct and visual proof, the

real-space observation of its broken rotational symmetry in the electronic structure at the atomic scale, has been a critical missing piece.

CsV<sub>2</sub>Se<sub>2</sub>O, a predicted *d*-wave altermagnet<sup>3</sup>, provides an exemplary platform to address this gap. Its V<sub>2</sub>O plane forms an anti-CuO<sub>2</sub> lattice<sup>13,34</sup> (Figs. 1a, b), making it a magnetic counterpart<sup>1,35,36</sup> to high-temperature superconducting cuprates and an ideal system to explore *d*-wave order originating from crystal symmetry without strong electron correlations. While previous studies on related compounds have confirmed key momentum-space features like alternating spin splitting and C<sub>2</sub>-symmetric Fermi surface (FS, Fig. 1c)<sup>13</sup>, the real-space electronic landscape is uncharted. In this work, we employ scanning tunneling microscopy (STM) to investigate CsV<sub>2</sub>Se<sub>2</sub>O at the atomic scale. We directly image the broken rotational symmetry through unidirectional static charge orders and electronic charging rings encircling spin defects. Quasiparticle interference (QPI) measurements independently reveal scattering wavevectors that confirm the alternating spin-polarized band structure. Furthermore, we discover a spin-density-wave (SDW) gap and an associated charge order. These combined observations offer the long-sought, direct real-space verification of *d*-wave altermagnetism and establish a material platform for visualizing its interplay with other emergent quantum orders.

### **Magnetic structure and SDW gap**

CsV<sub>2</sub>Se<sub>2</sub>O crystallizes in a layered tetragonal structure (Fig. 1a). Its spin configuration in the V<sub>2</sub>O plane leads to a vanishing net magnetization, similar to an antiferromagnet. Se atoms reside above and below the center of each V<sub>2</sub>O square, while Cs layers intercalate between neighboring V<sub>2</sub>Se<sub>2</sub>O layers. Within the spin-up (down) sublattice, the V-O bonds align along the *x* (*y*) direction (Fig. 1b). Connecting the opposite spin sublattices requires a non-relativistic spin group operation, [C<sub>2</sub>||C<sub>4z</sub>], which combines a 180° rotation in spin-space (C<sub>2</sub>) with a 90° real-space rotation about the *z*-axis (C<sub>4z</sub>). This operation reduces the symmetry of each spin sublattice from C<sub>4</sub> to C<sub>2</sub>. Previous ARPES and NMR studies<sup>13</sup> report two distinct magnitudes of magnetic moment for both spin-up and spin-down, forming a  $\sqrt{2} \times \sqrt{2}$  spin density wave (SDW) in the V<sub>2</sub>O plane (Fig. 1b), supported by a density-wave-like transition near 100 K observed in transport measurements<sup>37</sup>. The spin-defined environment from the four surrounding V atoms dictates the electronic state of each surface Se atom, thus driving the formation of a  $\sqrt{2} \times \sqrt{2}$  charge density wave (CDW, dashed box in Fig. 1b). Our STM measurements directly visualize this SDW-induced CDW on the cleaved surface (Fig. 1d, e). The inset of Fig. 1d shows both Bragg peaks and  $\sqrt{2} \times \sqrt{2}$  CDW peaks in the fast Fourier transformation (FFT) result. The measured lattice constant (*a*=4.09 Å) agrees with the reported values for CsV<sub>2</sub>Se<sub>2</sub>O single crystals<sup>34</sup>. Uniform *dI/dV* spectra acquired across the clean Se surface show a consistent SDW gap of ~ 70 meV (upper panel of Fig. 1f).

In a large-scale STM topographic image (Fig. 1e), strip-like features (orange arrows) and two types of defects are observed on the Se surface. These strip-like features correspond to domain walls along the (110) direction. Both Defect 1 and Defect 2 exhibit a cross-shaped morphology (see Extended Data Fig. 1), with Defect 1 located on the domain walls and Defect 2 off the walls.  $dI/dV$  spectra acquired at Defect 1 and Defect 2 reveal in-gap states at distinct energies ( $\sim 20$  meV for Defect 1,  $\sim 40$  meV for Defect 2, lower panel of Fig. 1f).

### Rotational-symmetry-breaking states

Real-space rotational-symmetry breaking serves as conclusive proof of altermagnetism. The first rotational-symmetry-breaking state is observed around Defect 1. Defect 1 induces a quasi-one-dimensional (quasi-1D) static charge order that propagates into neighboring domains along either the  $x$  or  $y$  direction (Figs. 2a, b). This charge order, with a period of  $2a_0$  (twice the Se square lattice constant), aligns with both the  $C_2$  symmetry and the V-O bond direction of the host spin sublattice. In Fig. 2a, domain walls manifest as dark strips, while in the lower-energy  $dI/dV$  map (Fig. 2b), they appear as bright strips. This contrast reversal confirms the electronic origin of the domain walls. The static charge orders exhibit identical orientations on the same domain wall but adopt orthogonal directions on adjacent walls (double-headed arrows, Fig. 2b). These findings are reproducible across different samples and at various locations on the same sample (Extended Data Fig. 2).

$dI/dV$  maps at two characteristic energies reveal both defect-induced static order and QPI patterns (Fig. 2b, c). Their corresponding FFT results reveal three wavevectors: the static charge order wavevector  $q_0$  (induced by Defect 1, Fig. 2d), and the QPI wavevectors  $q_1$  and  $q_2$ , presented in Fig. 2d and 2e, respectively.  $q_1$  and  $q_2$  exhibit distinct arc-like shapes, convex for  $q_1$ , and concave for  $q_2$ , along with different energy dependencies. Inverse fast Fourier transformation (IFFT) results demonstrate that the real-space signals of  $q_0$  and  $q_1$  are strictly colocalized around Defect 1 on the domain wall, with  $q_0$  appearing straight and  $q_1$  rounded (Figs. 2f, g). In contrast, the  $q_2$  is confined around Defect 2 within the domains (Fig. 2h). This spatial distribution indicates that domain-wall-bound Defect 1 simultaneously induces the quasi-1D static order ( $q_0$ ) and acts as the scattering center for  $q_1$ , while Defect 2 inside the domains is the exclusive scattering center for  $q_2$ .

The unidirectional nature of all observed static order and QPI patterns (Figs. 2f-h) directly demonstrates rotational-symmetry breaking in real space. This is consistent with their origin in the material's  $d$ -wave altermagnetism, which we analyze in the following section.

Another symmetry-breaking state emerges as a charging ring induced by Defect 2 within the domains. We first characterize the structure of Defect 2. STM topography (Fig. 3a) reveals two typical forms of Defect 2: one with a smaller and one with a larger

apparent size. The schematic in Fig. 3b depicts the cross-shaped, smaller variant, featuring a central Se vacancy on the surface and associated spin defects on two nearest-neighbor V-atoms (blue dashed circles). Given that each  $V_2O$  layer is sandwiched between two Se layers (Fig. 1a), equivalent spin defects can be induced by a Se vacancy in the bottom layer. We attribute the larger, checkerboard-like Defect 2 in Fig. 3a to such a bottom-layer vacancy (Extended Data Fig. 3), analogous to the case of Fe vacancy in  $FeSe$ <sup>38</sup>.

A series of ellipse-shaped charging rings is clearly resolved in  $dI/dV$  maps at the characteristic energy of Defect 2 (Fig. 3c). These  $C_2$ -symmetric ellipses have their long axes aligned along either the  $x$  or  $y$  direction, matching the symmetry of the spin-up or spin-down sublattices (Fig. 3b). To highlight their spatial relationship with the defects, the rings are superimposed on a current map where only defects are visible (Fig. 3d). All rings are localized around Defect 2 and confined within individual domains, never crossing domain walls. This indicates that the rings are induced by the spin defects of Defect 2 and inherently inherit the symmetry of the host spin sublattice. The rings are displaced from the center of Defect 2, likely due to the inequivalence of the two V-atom spins associated with the Se vacancy (Fig. 3b). The coexistence of rings with long axes along both  $x$  and  $y$  in Fig. 3c confirms that the  $C_2$  symmetry is an intrinsic material property, ruling out artifacts from the STM tip shape. Within a single domain, rings with orthogonal orientations can both be observed (Fig. 3d). This can be understood from the spin sublattice configuration: each Se vacancy is surrounded by two spin-up and two spin-down V atoms, with the two V-atom pairs being mutually perpendicular. Consequently, defects (and thus their associated charging rings) linked to both spin sublattices can form within the same domain.

### Origin of ellipse charging ring

Figure 3e, f present close-up  $dI/dV$  maps of the charging ring around Defect 2. Spatially resolved spectroscopy along the ring's long axis reveals that the defect-state peak at  $\sim 40$  meV (also in Fig. 1f) shifts to lower energy with increasing lateral distance from the defect (Fig. 3g, h). This shift is consistent with the tip-induced band bending<sup>39,40</sup>: a downward band bending moves the defect state, initially slightly above  $E_F$  within the SDW gap, below  $E_F$  (Fig. 3i). The magnitude of band bending increases with smaller tip bias ( $V$ ) and smaller tip-defect distance. Consequently, in a  $dI/dV$  map at a fixed bias, the charging ring appears at the lateral position where the defect state  $E_D$  is bent across  $E_F$ ; a lower bias produces a larger ring (Extended Data Fig. 4). Conversely, at a greater lateral distance, a lower bias is required to achieve the same band bending, explaining the observed energy shift in the spectra (Figs. 3g, h). Notably, the peak shifts more rapidly when moving away from Defect 2 along the short axis of the ring (Extended Data Fig. 5), indicating that the band bending decays faster along one principal direction ( $x$  or  $y$ ) than the other.

This directional anisotropy directly reflects the rotational-symmetry breaking of the charging rings, which fundamentally stems from the  $C_2$  symmetry of the spin sublattice and the corresponding anisotropic band structure.

### Origin of unidirectional static order

We now examine the unidirectional static charge order that emerges along either the  $x$  or  $y$  direction around Defect 1 on the domain walls. A zoom-in  $dI/dV$  map reveals its characteristic W-shaped profile (Fig. 4a). The proposed atomic structure (Fig. 4b) indicates that, for charge order along  $x$ , a spin-down V-O chain lies at the center of each blue W-shaped shaded area; for order along  $y$ , a spin-up V-O chain centers the light red shaded W-shaped area. The W-shaped pattern results from the superposition of the V-O chains (period  $2a_0$ ) and the  $\sqrt{2}\times\sqrt{2}$  CDW on the Se layer. Like the charging rings, this order originates from spin defects, and its quasi-1D character likewise stems from the  $C_2$  symmetry of the spin sublattices.

Critically, all quasi-1D static charge orders on the same domain wall share the same orientation (Fig. 2f). We propose that a given domain wall hosts only one type of spin defect (spin-up *or* spin-down). As depicted in Fig. 4b, an altermagnetic domain wall is formed by two columns of spin-down V atoms. Consequently, only spin-down defects can be induced by a surface Se vacancy on that wall, leading to static charge order exclusively along  $x$  (blue shaded area). Adjacent domain walls, composed of opposite spins, therefore exhibit orthogonal charge orders. STS spectra along the charge order reveal intriguing electronic states near 20 meV (Figs. 4d, e). The defect state of Defect 1 splits into two branches away from the defect site (Figs. 4c-e). The unsplit center of this state is also offset from the Se-vacancy site (red cross and dashed line in Figs. 4c, e), a displacement attributed to the inequivalence of the two V-atom spins associated with the vacancy. This spatial distribution is not a tip-induced artifact, as confirmed by spectra taken at fixed locations with varying setpoints (Extended Data Fig. 6).

### Origin of observed QPIs

The convex  $q_1$  and concave  $q_2$  wavevectors (Figs. 2d, e and 5a, f) characterize the distinct QPI patterns. To understand their origin, we performed self-correlation simulations based on the spin-resolved Fermi surface (FS) from ARPES<sup>13</sup> (Fig. 5b). The simulation considering only spin-conserved scattering (Fig. 5c) reproduces the observed wavevector  $q_2$  perfectly. In contrast, the simulation that includes spin-flip processes (Fig. 5d) yields additional features, as highlighted by the gray circles. Crucially, these extra features are absent in our experimental QPI data (Fig. 5a). This agreement demonstrates conclusively that  $q_2$  arises from spin-conserved scattering between FS contours of the same spin orientation (red arrow in Fig. 5b). While magnetic impurities allow spin-flip processes, the initial and final spin states remain orthogonal in  $d$ -wave altermagnet and contribute no interference, analogous to the case of

topological insulators.<sup>41-43,44</sup>  $q_2$  is observable in QPI because its energy lies near the SDW gap edge. The measured dispersion of  $q_2$  (from 35-65 meV) exhibits electron-like behavior (Fig. 5e), consistent with both band structure calculations and ARPES data<sup>13</sup> (Extended Data Fig. 7).

The QPI wavevector  $q_1$  (Fig. 5f), coexisting with the static charge order  $q_0$ , is distinct from  $q_2$  in both real-space location and energy, appearing around Defect 1 within the 16-36 meV range (Figs. 2f, g). To understand  $q_1$ , the FS folding induced by the  $q_0$  charge order (period  $2a_0$ , Fig. 5g) must be considered. However, self-correlation simulations (Fig. 5g inset) based on this folded FS fail to reproduce the observed  $q_1$ .

A consistent picture emerges by considering the energy hierarchy of the gap-opening: while the  $\sqrt{2}\times\sqrt{2}$  SDW opens a uniform gap across the FS<sup>13</sup>, the static charge order ( $q_0$ ) introduces a secondary gap only at higher energy (Fig. 5h). Therefore, within the SDW gap at the energies relevant to  $q_1$ , the electronic structure is effectively governed by the bands folded solely by the static charge order (bands and FS contours denoted by dashed lines in Figs. 5h, i). Simulations based on this picture (Fig. 5j) successfully reproduce  $q_1$ . The extracted dispersions (Fig. 5k) confirm the non-dispersing nature of  $q_0$ . As for  $q_1$ , its appearance within a narrow energy range precludes a definitive dispersion analysis.

While the spin-conserved nature of the quasiparticle scattering, consistent with a prior report<sup>6</sup>, is confirmed by our analysis, the key advance of our work lies in the direct real-space observation of rotational-symmetry breaking. Although the Fourier transformations of  $q_1$  and  $q_2$ , which spatially average signals from multiple defects, exhibit an apparent  $C_4$  symmetry (Figs. 2d, e and 5a, f), the QPI maps around individual defects reveal clearly unidirectional interference patterns (Figs. 2g, h). This defect-resolved unidirectionality, together with the other symmetry-breaking electronic states—the static charge order and the anisotropic charging rings—provides unambiguous real-space evidence for altermagnetism, moving beyond the established momentum-space signatures.

## Outlook

Our atomic-scale visualization of altermagnetism not only confirms the long-predicted rotational-symmetry breaking, but further reveals how this fundamental symmetry lowering manifests in distinct unidirectional electronic states. These real-space patterns encode the underlying alternating spin texture and its coupling to the lattice, offering a new window into the microscopic interplay between spin, charge, and crystal symmetry in altermagnets.

$\text{CsV}_2\text{Se}_2\text{O}$  thus emerges as a clean prototype for  $d$ -wave altermagnetism. Intriguingly, symmetry-breaking electronic orders resembling those observed here are also found in cuprate superconductors, where they are linked to the pseudogap<sup>45,46</sup> and unconventional superconductivity<sup>47</sup>. In  $\text{CsV}_2\text{Se}_2\text{O}$ , however, the band structure with  $d$ -

wave spin-splitting originates directly from crystal symmetry, providing a clean, correlation-light platform to disentangle symmetry-driven phenomena from strong correlation effects. The intimate coupling between altermagnetism and charge degrees of freedom suggests that related materials may host emergent phases such as spin-triplet superconductivity. A promising route is to interface such *d*-wave altermagnets with superconductors, where the spin-split Fermi surfaces could stabilize equal-spin pairing and thus generate spin-triplet superconductivity<sup>48</sup>, offering a materials-realizable pathway to this long-sought state.

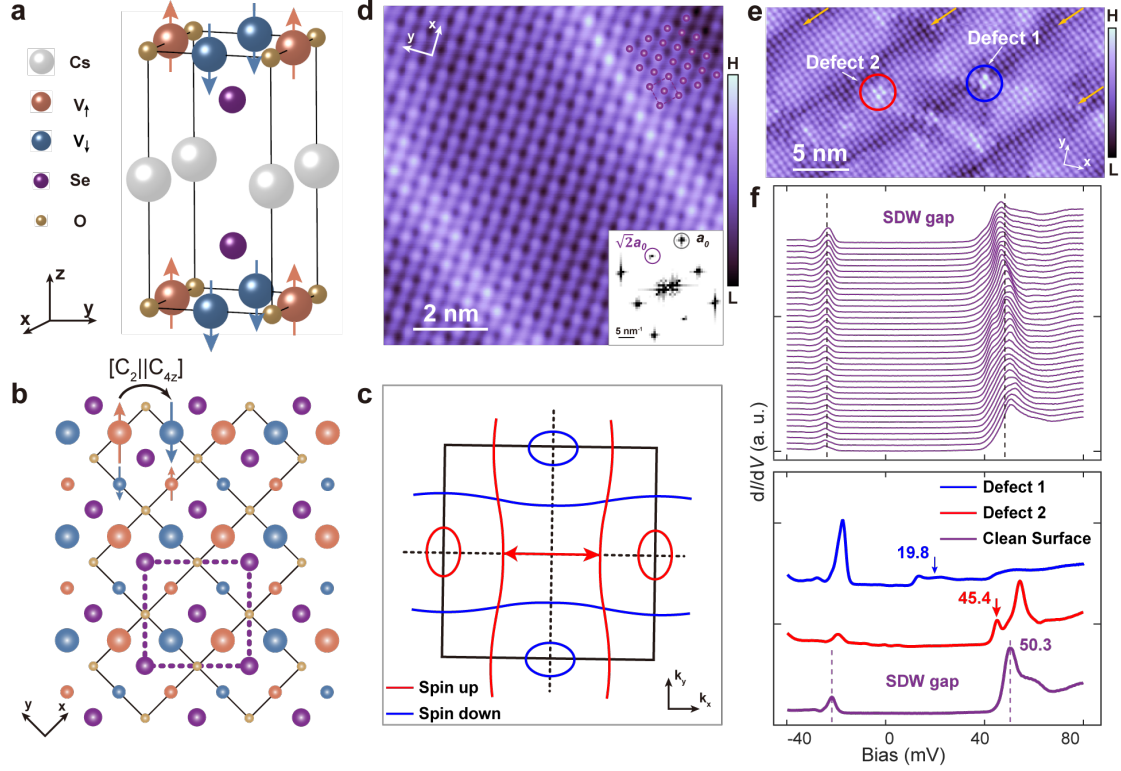


**Fig. 1 | Spin density wave gap and induced charge order in the altermagnet  $\text{CsV}_2\text{Se}_2\text{O}$ .** **a**, Crystal and magnetic structure of  $\text{CsV}_2\text{Se}_2\text{O}$ . Red and blue arrows indicate the up and down spins of the V atoms. **b**, Top view of the Se plane and  $\text{V}_2\text{O}$  plane. The size of the blue and red spheres indicates the magnitudes of the magnetic moments of the V atoms. Purple dashed square denotes one unit cell of the SDW-induced  $\sqrt{2} \times \sqrt{2}$  CDW on the Se surface. The opposite spin lattice is connected by the  $[C_2||C_{4z}]$  operation. **c**, Schematic Fermi surface with red (blue) lines indicating the constant energy contour of spin-up (down) electrons. Black lines indicate the first Brillouin zone. Red double-headed arrow indicates the spin-conserved scattering process. **d**, **e**, Atomically resolved STM topographic image of a cleaved Se surface (**c**:  $9 \text{ nm} \times 9 \text{ nm}$ , set point  $V_s = 30 \text{ mV}$ ,  $I_t = 200 \text{ pA}$ ; **d**:  $30 \text{ nm} \times 15 \text{ nm}$ , set point  $V_s = 60 \text{ mV}$ ,  $I_t = 800 \text{ pA}$ ). Purple spheres in **c** denote the Se square lattice. Inset of **c**: the fast Fourier transformation result of **c**, gray and purple circles denote the Bragg peak of the Se square lattice and the  $\sqrt{2} \times \sqrt{2}$  CDW, respectively. Yellow arrows in **d** indicate domain walls. Red and blue circles in **d** indicate a defect inside the domain (Defect 1) and a defect on the domain wall (Defect 2), respectively. **f**, Top: A series of  $dI/dV$  spectra (set point  $V_s = 80 \text{ mV}$ ,  $I_t = 800 \text{ pA}$ ) taken on the clean surface. Black dashed lines indicate a uniform SDW gap. Bottom:  $dI/dV$  spectra (set point  $V_s = 80 \text{ mV}$ ,  $I_t = 800 \text{ pA}$ ) taken on clean surface, defect 1 and defect 2, respectively. Purple dashed lines indicate the SDW gap on the clean surface, and red and blue arrows denote defect-induced electronic states.

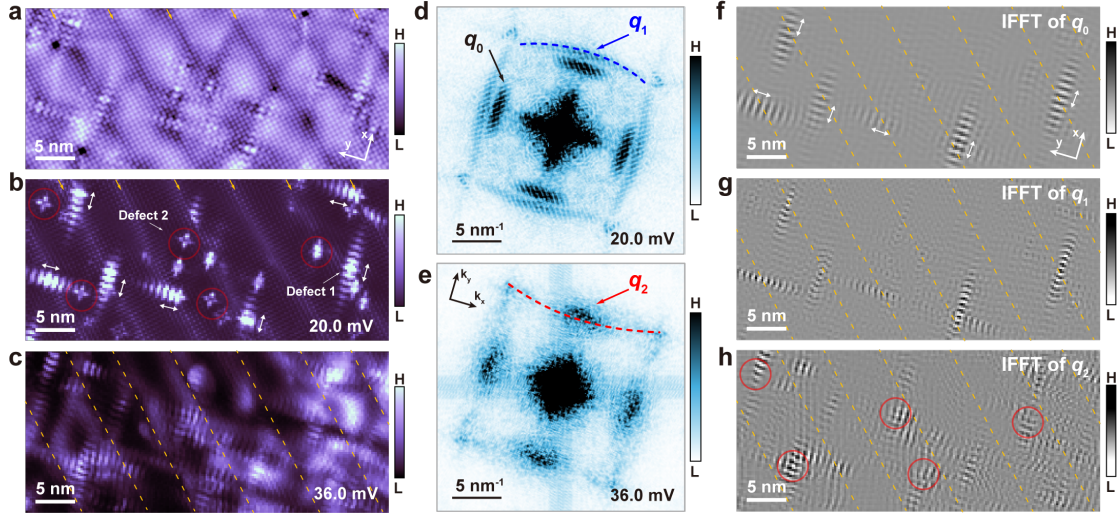


**Fig. 2 | Quasi-1D static charge order and quasiparticle interference pattern in  $\text{CsV}_2\text{Se}_2\text{O}$ .** **a**, STM topographic image of a Se surface ( $45 \text{ nm} \times 20 \text{ nm}$ , set point  $V_s = 50 \text{ mV}$ ,  $I_t = 500 \text{ pA}$ ). **b**, **c**,  $dI/dV$  mapping of the Se surface ( $45 \text{ nm} \times 20 \text{ nm}$ , set point  $V_s = 80 \text{ mV}$ ,  $I_t = 1.2 \text{ nA}$ ) at the energy of  $20.0 \text{ mV}$  (**b**) and  $36.0 \text{ mV}$  (**c**). Red circles in **b** indicate defect 2, white double-headed arrows indicate defect 1 and the quasi-1D static charge order around it. Yellow arrows and dashed lines in **a**, **b**, **c** denote the domain walls. Static charge orders are aligned identically on the same domain wall but orthogonally on neighboring walls. **d**, **e**, The symmetrized Fast Fourier transformation result of **b**(**d**) and **c**(**e**). Black arrow indicates the static charge order wavevector  $q_0$ , blue (red) arrow and dashed line indicate the quasiparticle interference wavevector  $q_1$  ( $q_2$ ). **f**, **g**, **h**, Inverse fast Fourier transformation result of static charge order wavevector  $q_0$  (**f**), QPI wavevector  $q_1$  (**g**) and  $q_2$  (**h**). Yellow dashed lines, white double-headed arrows and red circles retain their meanings as defined in **a–c**. The scattering centers of  $q_1$  and  $q_2$  are Defect 1 (on the domain wall) and Defect 2 (within the domain), respectively. The  $q_2$ -related scatterings are marked red circles.

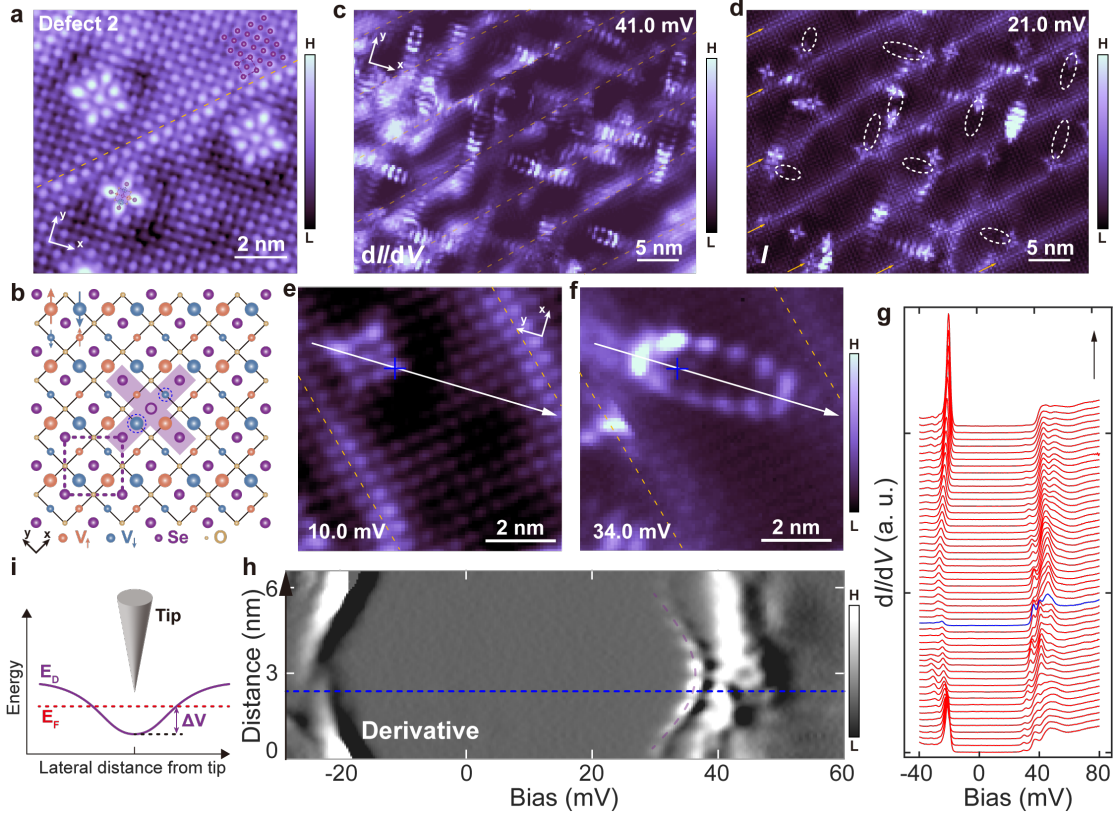


**Fig. 3 | Charging ring with broken rotational symmetry in the altermagnetic state.** **a**, STM topographic image of Defect 2 (10 nm  $\times$  10 nm, set point  $V_s = 10$  mV,  $I_t = 200$  pA). Purple spheres denote the Se square lattice. **b**, Atomic structure of Defect 2. The cross-shaped purple shaded area corresponds to the composite defect site (atoms assembled in **a**, which is defined by a central Se vacancy (purple circle) and a spin defect on its nearest-neighbor V atoms (two blue dashed circles). A purple dashed square denotes a unit cell of the  $\sqrt{2} \times \sqrt{2}$  CDW on Se surface. Two additional defects with larger apparent sizes are of the same type as Defect 2 but reside in deeper atomic layers (see SI-x for details). **c**,  $dI/dV$  mapping (40 nm  $\times$  30 nm, set point  $V_s = 60$  mV,  $I_t = 1.2$  nA) at the energy of 41.0 mV. Rotational-symmetry-breaking charging rings are clearly visualized. **d**, Current mapping (40 nm  $\times$  30 nm, set point  $V_s = 60$  mV,  $I_t = 1.2$  nA) at an identical FOV with **c** at the energy of 21.0 mV. White dashed circles indicate the charging rings in **c**. **e**, **f**,  $dI/dV$  mapping of the charging ring around defect 1 (7.5 nm  $\times$  7.5 nm, set point  $V_s = 60$  mV,  $I_t = 1.2$  nA) at the energy of 10.0 mV (**e**) and 32.0 mV (**f**). Yellow dashed lines and arrows in **a-f** indicate the domain walls. **g**, A series of STS spectra taken along the white arrow in **e** and **f** (set point  $V_s = 80$  mV,  $I_t = 800$  pA). **h**, False color image of the derivative of the  $dI/dV$  spectra in **g**. Blue line and dashed line in **g** and **h** indicate the spectrum taken at the blue cross position in **e** and **f**. **i**, Schematic of tip-induced band bending. Purple (dashed) lines in **i** and **h** indicate the bended defect state  $E_D$ .

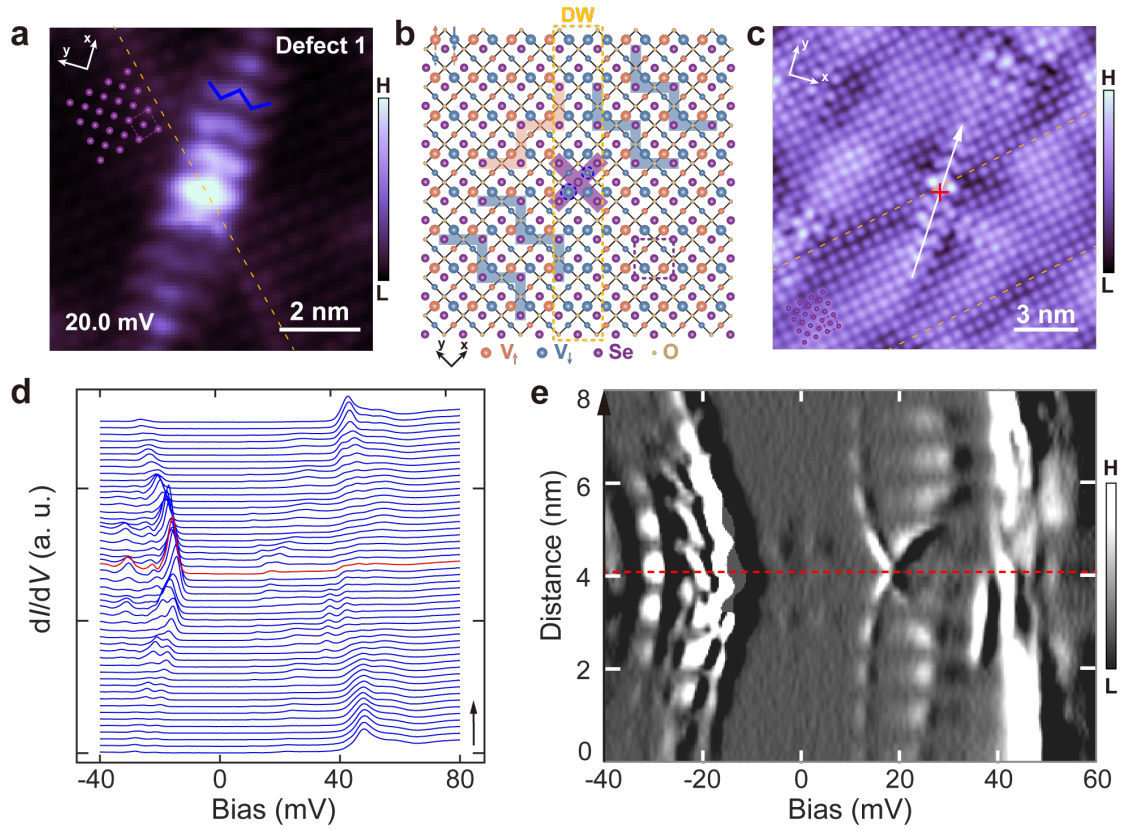


**Fig. 4 | Unidirectional electronic states induced by defect on the altermagnetic domain wall.** **a**,  $dI/dV$  mapping ( $10\text{ nm} \times 10\text{ nm}$ , set point  $V_s = 60\text{ mV}$ ,  $I_t = 1.2\text{ nA}$ ) of quasi-1D static charge order induced by a defect on the domain wall (Defect 1) at the energy of  $20.0\text{ mV}$ . Yellow dashed line indicates the domain wall. W-shaped blue line denotes the static charge order. Purple spheres denote the Se square lattice. **b**, Atomic structure of the altermagnetic domain wall. The size of the red (blue) spheres indicates the magnitude of the magnetic moments of the spin-up (down) of V atoms. Yellow dashed rectangle indicates the altermagnetic domain wall. W-shaped blue shaded areas indicate the surface highlighted Se atoms corresponding to the quasi-1D static charge order in **a**. W-shaped light red shaded area indicates the possible static charge order in the orthogonal direction. Purple dashed lines indicate a unit cell of the  $\sqrt{2} \times \sqrt{2}$  SDW-induced CDW on the Se surface. **c**, STM topographic image of quasi-1D static charge order ( $10\text{ nm} \times 10\text{ nm}$ , set point  $V_s = 60\text{ mV}$ ,  $I_t = 1.2\text{ nA}$ ). Yellow dashed lines and purple spheres retain their meanings in **a**. **d**, A series of  $dI/dV$  spectra taken along the white arrow in **c** (set point  $V_s = 80\text{ mV}$ ,  $I_t = 800\text{ pA}$ ). **e**, False color image of the derivative of the  $dI/dV$  spectra in **d**. Red (dashed) line in **d** and **e** indicates the spectrum taken at the point denoted by the red cross in **c**.

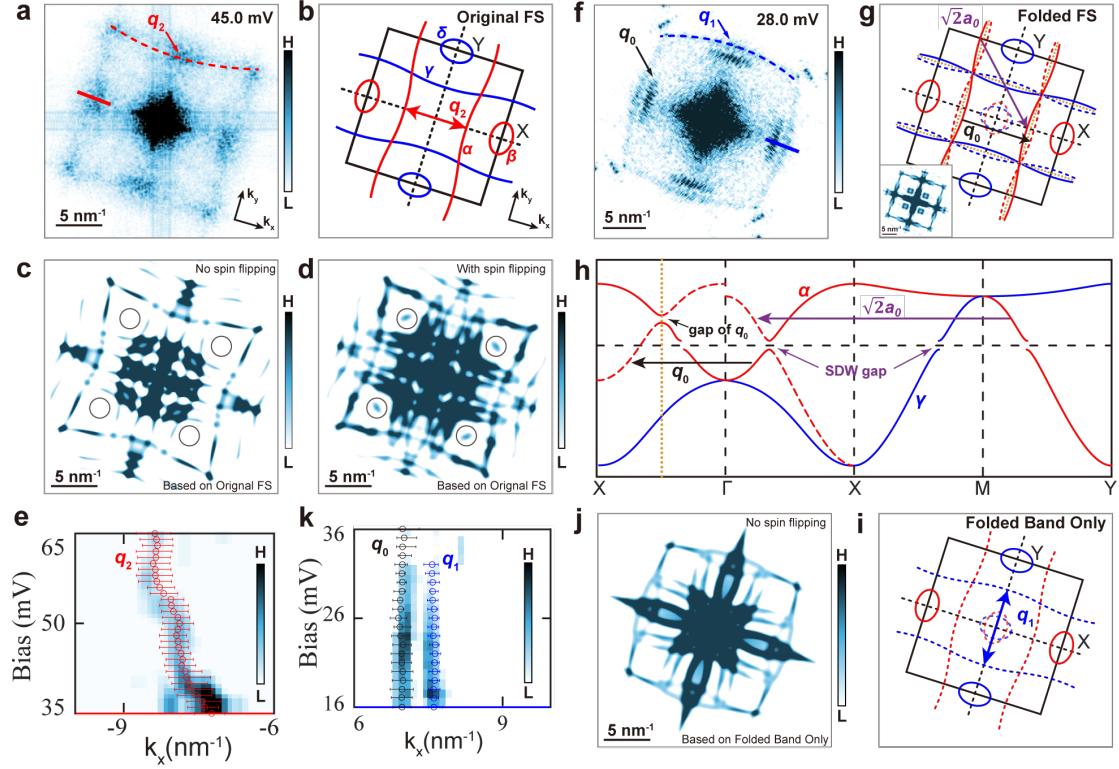


**Fig. 5 | Origin of observed QPI in spin-conserved scattering process.** **a**, Fourier transformation of  $dI/dV$  mapping ( $45 \text{ nm} \times 20 \text{ nm}$ ,  $V_s = 80 \text{ mV}$ ,  $I_t = 1.2 \text{ nA}$ ) at  $45.0 \text{ meV}$ . Red dashed line and arrow indicate the QPI wavevector  $q_2$ . **b**, Schematic Fermi surface with red (blue) lines indicating the constant energy contour of spin-up (down) electrons. Black lines indicate the first Brillouin zone. Red double-headed arrow indicates the spin-conserved scattering process for  $q_2$ . **c**, **d**, Simulated QPI wavevectors based on the Fermi surface in **b** with (**d**) and without (**c**) spin flipping process. **e**, Dispersion of  $q_2$  extracted from the red cut in **a**. Red circles with error bars indicate the measured wavevectors at each energy. **f**, Fourier transformation of  $dI/dV$  mapping ( $42 \text{ nm} \times 42 \text{ nm}$ ,  $60 \text{ mV}$ ,  $1.2 \text{ nA}$ ) at  $28.0 \text{ meV}$ . Black and blue arrows indicate the static order wavevector  $q_0$  and QPI wavevector  $q_1$ . **g**, Fermi surface folded by  $q_0$  with red (blue) dashed lines indicating the constant energy contour of folded band of spin-up (down) electrons. Orange dashed line indicates the folding boundary of  $q_0$ . Inset: Simulated QPI wavevectors based on **g**. **h**, Schematic of folded energy bands. Red and blue (dashed) lines indicate spin-up and spin-down (folded) energy bands. Black and purple arrows in **g** and **h** indicate the charge order wavevector  $q_0$  and the SDW wavevector. Only one branch of the folded band from  $q_0$  and SDW each is plotted for clarity. **i**, Fermi surface with only folded bands. Blue double-headed arrow indicates spin-conserved scattering process corresponding to  $q_1$ . **j**, Simulated QPI wavevectors based on **i** without the spin flipping process. **k**, Dispersion of  $q_0$  and  $q_1$  extracted from the blue cut in **f**. Black (blue) circles with error bars indicate the measured wavevectors  $q_0$  ( $q_1$ ) at each energy.

## References

- 1 Smejkal, L., Sinova, J. & Jungwirth, T. Emerging Research Landscape of Altermagnetism. *Phys. Rev. X* **12**, 040501 (2022).
- 2 Smejkal, L., González-Hernández, R., Jungwirth, T. & Sinova, J. Crystal time-reversal symmetry breaking and spontaneous Hall effect in collinear antiferromagnets. *Sci. Adv.* **6**, eaaz8809 (2020).
- 3 Ma, H. Y. *et al.* Multifunctional antiferromagnetic materials with giant piezomagnetism and noncollinear spin current. *Nat. Commun.* **12**, 2846 (2021).
- 4 González-Hernández, R. *et al.* Efficient Electrical Spin Splitter Based on Nonrelativistic Collinear Antiferromagnetism. *Phys. Rev. Lett.* **126**, 127701 (2021).
- 5 Smejkal, L. *et al.* Giant and Tunneling Magnetoresistance in Unconventional Collinear Antiferromagnets with Nonrelativistic-Momentum. *Phys. Rev. X* **12**, 011028 (2022).
- 6 Zhang, F. Y. *et al.* Crystal-symmetry-paired spin-valley locking in a layered room-temperature metallic altermagnet candidate. *Nat. Phys.* **21**, 760–767 (2025).
- 7 Krempasky, J. *et al.* Altermagnetic lifting of Kramers spin degeneracy. *Nature* **626**, 517–522 (2024).
- 8 Zhu, Y. P. *et al.* Observation of plaid-like spin splitting in a noncoplanar antiferromagnet. *Nature* **626**, 523–528 (2024).
- 9 Ding, J. Y. *et al.* Large Band Splitting in g-Wave Altermagnet CrSb. *Phys. Rev. Lett.* **133**, 206401 (2024).
- 10 Reimers, S. *et al.* Direct observation of altermagnetic band splitting in CrSb thin films. *Nat. Commun.* **15**, 2116 (2024).
- 11 Lee, S. *et al.* Broken Kramers Degeneracy in Altermagnetic MnTe. *Phys. Rev. Lett.* **132**, 036702 (2024).
- 12 Osumi, T. *et al.* Observation of a giant band splitting in altermagnetic MnTe. *Phys. Rev. B* **109**, 115102 (2024).
- 13 Jiang, B. *et al.* A metallic room-temperature d-wave altermagnet. *Nat. Phys.* **21**, 754–759 (2025).
- 14 Liu, P. F. *et al.* Spin-Group Symmetry in Magnetic Materials with Negligible Spin-Orbit Coupling. *Phys. Rev. X* **12**, 021016 (2022).
- 15 Smejkal, L., Sinova, J. & Jungwirth, T. Beyond Conventional Ferromagnetism and Antiferromagnetism: A Phase with Nonrelativistic Spin and Crystal Rotation Symmetry. *Phys. Rev. X* **12**, 031042 (2022).
- 16 Feng, Z. X. *et al.* An anomalous Hall effect in altermagnetic ruthenium dioxide. *Nat. Electron.* **5**, 735–743 (2022).
- 17 Zhu, Z. H. *et al.* Anomalous Antiferromagnetism in Metallic RuO<sub>2</sub> Determined by Resonant X-ray Scattering. *Phys. Rev. Lett.* **122**, 017202 (2019).
- 18 Hiraishi, M. *et al.* Nonmagnetic Ground State in RuO<sub>2</sub> Revealed by Muon Spin Rotation. *Phys. Rev. Lett.* **132**, 166702 (2024).
- 19 Fedchenko, O. *et al.* Observation of time-reversal symmetry breaking in the band structure of altermagnetic RuO<sub>2</sub>. *Sci. Adv.* **10**, eadj4883 (2024).

- 20 Bai, H. *et al.* Observation of Spin Splitting Torque in a Collinear  
Antiferromagnet RuO<sub>2</sub>. *Phys. Rev. Lett.* **128**, 197202 (2022).
- 21 Zhou, Z. Y. *et al.* Manipulation of the altermagnetic order in CrSb via crystal  
symmetry. *Nature* **638** (2025).
- 22 Bose, A. *et al.* Tilted spin current generated by the collinear antiferromagnet  
ruthenium dioxide. *Nat. Electron.* **5**, 267–274 (2022).
- 23 Betancourt, R. D. G. *et al.* Spontaneous Anomalous Hall Effect Arising from an  
Unconventional Compensated Magnetic Phase in a Semiconductor. *Phys. Rev.  
Lett.* **130**, 036702 (2023).
- 24 Mazin, I. I. *et al.* Prediction of unconventional magnetism in doped FeSb<sub>2</sub>. *Proc.  
Natl. Acad. Sci. U.S.A.* **118**, e2108924118 (2021).
- 25 Bai, L. *et al.* Altermagnetism: Exploring New Frontiers in Magnetism and  
Spintronics. *Adv. Funct. Mater.* **34** (2024).
- 26 Song, C. *et al.* Altermagnets as a new class of functional materials. *Nat. Rev.  
Mater.* **10**, 473–485 (2025).
- 27 Chen, H. Y. *et al.* Emerging Antiferromagnets for Spintronics. *Adv. Mater.* **36**,  
2310279 (2024).
- 28 Kriegner, D. *et al.* Multiple-stable anisotropic magnetoresistance memory in  
antiferromagnetic MnTe. *Nat. Commun.* **7**, 11623 (2016).
- 29 Brinkman, W. F. & Elliott, R. J. Theory of Spin-Space Groups. *Proc. R. Soc. A.*  
**294**, 343–358 (1966).
- 30 Litvin, D. B. & Opechowski, W. Spin Groups. *Physica* **76**, 538–554 (1974).
- 31 Litvin, D. B. Spin Point Groups. *Acta Crystallogr. Sec. A* **33**, 279–287 (1977).
- 32 Xiao, Z. Y. *et al.* Spin Space Groups: Full Classification and Applications. *Phys.  
Rev. X* **14**, 031037 (2024).
- 33 Chen, X. B. *et al.* Enumeration and Representation Theory of Spin Space  
Groups. *Phys. Rev. X* **14**, 031038 (2024).
- 34 Lin, H. *et al.* Structure and physical properties of CsV<sub>2</sub>Se<sub>2-x</sub>O and V<sub>2</sub>Se<sub>2</sub>O. *Phys.  
Rev. B* **98**, 075132 (2018).
- 35 Wu, C. J., Sun, K., Fradkin, E. & Zhang, S. C. Fermi liquid instabilities in the  
spin channel. *Phys. Rev. B* **75**, 115103 (2007).
- 36 Borzi, R. A. *et al.* Formation of a nematic fluid at high fields in Sr<sub>3</sub>Ru<sub>2</sub>O<sub>7</sub>.  
*Science* **315**, 214–217 (2007).
- 37 Bai, J. L. *et al.* Absence of long-range order in the vanadium oxychalcogenide  
KV<sub>2</sub>Se<sub>2</sub>O with nontrivial band topology. *Phys. Rev. B* **110**, 165151 (2024).
- 38 Bu, K. L. *et al.* Study of intrinsic defect states of FeSe with scanning tunneling  
microscopy. *Phys. Rev. B* **100**, 155127 (2019).
- 39 Marczinowski, F. *et al.* Local electronic structure near Mn acceptors in InAs:  
Surface-induced symmetry breaking and coupling to host states. *Phys. Rev. Lett.*  
**99**, 157202 (2007).
- 40 Nguyen, G. D. *et al.* 3D Imaging and Manipulation of Subsurface Selenium  
Vacancies in PdSe<sub>2</sub>. *Phys. Rev. Lett.* **121**, 086101 (2018).
- 41 Beidenkopf, H. *et al.* Spatial fluctuations of helical Dirac fermions on the  
surface of topological insulators. *Nat. Phys.* **7**, 939–943 (2011).

- 42 Okada, Y. *et al.* Direct Observation of Broken Time-Reversal Symmetry on the  
Surface of a Magnetically Doped Topological Insulator. *Phys. Rev. Lett.* **106**,  
206805 (2011).
- 43 Sessi, P. *et al.* Signatures of Dirac fermion-mediated magnetic order. *Nat.*  
*Commun.* **5**, 5349 (2014).
- 44 Hu, H. R., Wan, X. G. & Chen, W. Quasiparticle interference in altermagnets.  
*Phys. Rev. B* **111**, 035132 (2025).
- 45 Lawler, M. J. *et al.* Intra-unit-cell electronic nematicity of the high- $T_c$  copper-  
oxide pseudogap states. *Nature* **466**, 347–351 (2010).
- 46 Hamidian, M. H. *et al.* Atomic-scale electronic structure of the cuprate  $d$ -  
symmetry form factor density wave state. *Nat. Phys.* **12**, 150–156 (2016).
- 47 Ye, S. S. *et al.* The emergence of global phase coherence from local pairing in  
underdoped cuprates. *Nat. Phys.* **19**, 1301–1307 (2023).
- 48 Maeda, K. *et al.* Classification of pair symmetries in superconductors with  
unconventional magnetism. *Phys. Rev. B* **111**, 144508 (2025).

## Methods

### Sample preparation

Single crystals of CsV<sub>2</sub>Se<sub>2</sub>O were grown using a flux method with CsSe as the flux. The starting materials of Cs, Se, V, and V<sub>2</sub>O<sub>5</sub>, mixed in a molar ratio of CsV<sub>2</sub>Se<sub>2</sub>O: CsSe = 1:5, were loaded into an alumina crucible. The crucible was sealed in an evacuated quartz tube and pre-reacted at 40 °C for 1 hour. Subsequently, the quartz tube was heated slowly to 1000 °C, at which held for 10 hours to ensure homogenization, and then slowly cooled to 650 °C at a rate of 2 °C/h. Finally, the CsV<sub>2</sub>Se<sub>2</sub>O crystals were separated from the excess flux by centrifugation.

### STM Measurements

STM measurements were carried out in a low-temperature STM system (Unisoku 1200). A polycrystalline PtIr STM tip was calibrated on Ag island. STS data were taken by standard lock-in method. The feedback loop is disrupted during data acquisition and the frequency of oscillation signal is 811.0 Hz. CsV<sub>2</sub>Se<sub>2</sub>O single crystal were cleaved at 77 K under ultra-high vacuum (with the pressure < 2×10<sup>-10</sup> Torr) and then transferred to STM head at 4 K.

### Data availability

All study data are included in the article and/or Extended Data.

### Acknowledgements

D.F. and L.Y. contributed equally to this work. We thank G. Jia, J. Yan, Y. Peng, Z. Hu and W. Dong for helpful discussions. The experimental work was supported by the National Natural Science Foundation of China (NNSFC, Grant No. 92365201), the National Key R&D Program of China (Grant No. 2022YFA1403103), NNSFC (Grants No. 12321004, No. 52388201, and No. 11427903), and Quantum Science and Technology-National Science and Technology Major Project (2021ZD0302402).

### Author Contributions

W.L. and Q.-K.X. conceived the research project. D.F. and K.X. performed the STM experiments with the assistance of Y.W., L.Y., Z.W. and Y.Y. grew the samples. W.L., D.F. and K.X. analyzed the data. W.L., D.F. wrote the manuscript with input from all other authors.